Gregory Wallace
School of Mechanical and Materials Engineering,
Washington State University,
Sloan Hall, Spokane St.,
Pullman, WA 99164
e-mail: gregory.wallace@wsu.edu

Carl Bunge
School of Mechanical and Materials Engineering,
Washington State University,
Sloan Hall, Spokane St.,
Pullman, WA 99164
e-mail: carl.bunge@wsu.edu

Jacob Leachman
Mem. ASME
School of Mechanical and Materials Engineering,
Washington State University,
Sloan Hall, Spokane St.,
Pullman, WA 99164
e-mail: jacob.leachman@wsu.edu

Konstantin I. Matveev[1]
Mem. ASME
School of Mechanical and Materials Engineering,
Washington State University,
Sloan Hall, Spokane St.,
Pullman, WA 99164
e-mail: matveev@wsu.edu

Experimental and Numerical Investigation of a Miniature Additively Manufactured Vortex Tube

Ranque–Hilsch vortex tubes are simple devices that can produce a cooling effect using compressed air. A key advantage of vortex tubes is the lack of moving solid parts; however, their efficiencies are relatively low. The present study focuses on the development of a miniature variable-diameter tube using additive manufacturing. A metal-based 3D printing technique was utilized to fabricate this vortex tube monolithically. Computational fluid dynamics simulations employing software STAR-CCM+ *with a compressible Reynolds-Averaged Navier–Stokes (RANS) approach and the elliptic-blending lag k-epsilon turbulence model have been applied to model thermofluid processes inside the vortex tube, to good agreement with the experiment. A temperature decrease of 13.3 °C and a cooling power of approximately 4 W were experimentally achieved with a pressure ratio of 4 in the air at normal conditions. This result shows promise for the goal of utilizing additive manufacturing to design and build complex-geometry vortex tubes intended for use with cryogenic fluids.*
[DOI: 10.1115/1.4047527]

Keywords: energy systems, thermal systems

Introduction

Vortex tubes use a source of compressed gas to generate cooling beyond that of Joule–Thomson expansion without using any moving parts. Gas is injected tangentially through one or more nozzles, forming a vortex that propagates down the length of the tube. A standard vortex-tube configuration is shown in Fig. 1(*a*), and a more sophisticated version with a variable-diameter main tube is illustrated in Fig. 1(*b*). By inducing shear work in the periphery of the vortex, the central gas in the vortex expands, creating a cooling effect [1]. The shear work warms the peripheral gas which exits through the far end of the tube. The cold gas exits on the opposite end, near the inlets. Additional factors that can influence this temperature separation include fluid expansion in the vortex core due to high-speed rotation [2], turbulence-induced radial heat transport by compressible fluid particles [3], and even a sort of acoustic streaming [4].

The vortex-tube effect was first recorded by Ranque [5] and more deeply explored by Hilsch [6]. Though typically used for air, vortex tubes work with other gases, including helium which otherwise cannot cool via throttling at ambient temperature [7]. However, the use of liquids does not produce noticeable cooling [8]. Vortex tubes are typically applied for spot cooling (as a clean coolant for cutting tools) and spot heating (thermoforming plastics, drying systems) [9–11]. A simplified thermodynamic cycle analysis of vortex-tube systems has been developed in the past [12]. Cascade implementation of vortex tubes was also shown to make energy utilization more efficient [13].

When characterizing the performance of vortex tubes, the input parameters often include the pressure ratio (the ratio of absolute inlet pressure to absolute outlet pressure, usually on the cold side) and the cold fraction defined as the fraction of inlet gas leaving the cold outlet, which can be varied between 0 and 1. The primary output parameters are the temperatures at the outlets, which together with the cold fraction and flowrate, also define the cooling power.

To achieve high performance in simple vortex-tubes configurations, relatively long tubes are needed, with the length–diameter ratio of about 30. Many geometric configurations of vortex tubes have been examined for the purpose of improving cooling ability or making tubes more compact, such as the number of inlet nozzles [14], the tube length [7], the presence or absence of flow-straighteners (also called detwisters) at the outlets [15], and the shape of the tube [16]. One of the novel promising variations of vortex-tube geometries involves a conical section inside the main tube, as shown in Fig. 1(*b*) [17]; this geometry was adopted in the present study.

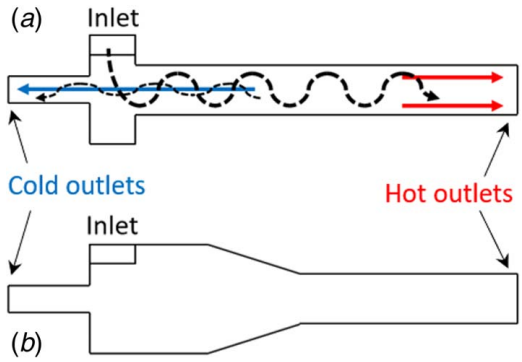

Fig. 1 (*a*) Cross section of a standard vortex tube with dashed lines indicating vortex-like fluid motion and (*b*) cross section of a cyclonic vortex tube similar to that used in this study

[1]Corresponding author.

Manuscript received February 15, 2020; final manuscript received June 6, 2020; published online August 5, 2020. Assoc. Editor: Vinod Narayanan.

Merkulov [3] provided a semi-empirical method to select geometric parameters for desired cooling conditions. However, most parametric tests of variable-geometry vortex tubes have been limited by the ability of conventional machining methods. Commercial vortex-tube system geometry tends to be complex, requiring multiple parts to be machined and sealed together and multiple assembly operations. As an example, an Exair 3215 model is made from nine machined components, one injection-molded part, and two O-rings, requiring four different materials plus one solder or braze material.

A variety of computational fluid dynamics (CFD) simulations have been used to model vortex tubes. Skye et al. [1] compared experimental cooling power with numerical predictions based on the standard k–ϵ and RNG k–ϵ turbulence models in an axisymmetric geometry, finding the standard k–ϵ model to be most accurate, though still off by up to 20%. They noted the need to decrease the inlet area of the CFD model by 23% for inlet pressure and mass flowrate to match. Dutta et al. [18] compared standard k–ϵ, RNG k–ϵ, standard k–ω, and SST k–ω turbulence models to experiment and found the standard k–ϵ most agreeing, although the standard k–ω and SST k–ω models did nearly as well. Eiamsa-ard and Promvonge [19] reviewed several other computational investigations, many using the standard k–ϵ model. In this study, we found that the elliptic-blending lag k–ϵ turbulence model gives superior agreement in comparison with the standard k–ϵ model for the miniature tube with a conical section, such as illustrated in Fig. 1(*b*). The relatively new elliptic-blending lag model uses a this-equation model which introduces a lag between the stress and strain tensors with a blending function required near walls [20,21]. It provides a good prediction for near-wall high-rotation flows with heat transfer [22].

The main practical motivation for the present study is to explore the possibility of using additive manufacturing, commonly known as 3D printing, to construct a miniature, monolithic vortex tube. Three-dimensional printing allows for complicated geometry, making rapid-prototyping of novel-shaped vortex tubes easier. It also allows for miniaturization, in this case down to several centimeters long and sub-centimeter wide, that can be useful for small-scale gas liquefaction or microfluidic systems, only limited by the precision of the printer. By employing only one material with no internal seals, risks of material incompatibility and uneven thermal expansion are lessened. The omission of internal seals also improves ease of testing in extreme temperatures, such as at cryogenic or high temperatures, where leak-checking is highly time-consuming. The work presented in this paper is a part of current efforts at Washington State University to develop a new generation of vortex tubes for cryogenic hydrogen systems [23].

Geometry and Fabrication

Since the main objectives of this study were only to demonstrate that a non-trivial vortex tube can be additively manufactured and be used to produce a cooling effect, the geometric proportions for the miniature variable-diameter vortex tube in this study were simply taken from a previous numerical investigation of novel vortex tubes with cyclonic extensions of vortex chambers [17]. The tube was scaled down to about 5 cm in length. The performance augmentation due to usage of a conical shape in the main tube was predicted to be about 15% in the previous study [17]. No other rationales were used in selecting the tube dimensions, and no optimization was performed in this work.

The main dimensions of the constructed single-inlet vortex tube are shown in Fig. 2. The material thickness of the tube was set to be at least 0.9 mm everywhere. A flow straightener comprising four fins was incorporated near the hot end. The inlet nozzle cross-sectional dimensions measured about 1.21 mm and 0.68 mm.

This vortex tube model was additively manufactured on a 3D Systems Pro 200 using direct metal laser sintering (DMLS) in Ti-Gr23(A), a grade of Ti-6Al-4V. Laser power was 167 W, scanning speed was 2400 mm/s, and the hatching space was 110 μmwith a 30 μm layer thickness. A photograph of the fabricated vortex tube weighing 5 g is shown in Fig. 3.

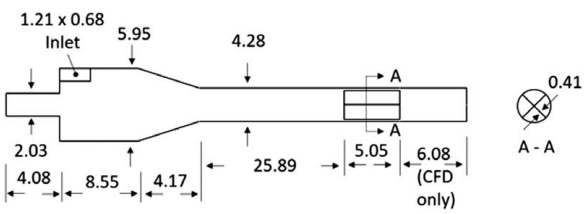

Fig. 2 Schematic and main internal dimensions of printed vortex tube. Cruciform flow straightener shown in cross-sectional A-A. Dimensions are in millimeters.

Experimental Setup and Procedure

An experimental setup designed for testing vortex tubes of various sizes was employed in this study (Fig. 4). For attaching the 3D- printed miniature vortex tube, connections made use of soft, flexible PVC tubing sealed with silicone epoxy. Type-K thermocouples were used to measure temperature with a sheathed thermocouple at the inlet (using a thermocouple pass-through fitting) and wire thermocouples at the outlets with an absolute uncertainty of ±2.2 °C and comparative uncertainty of ±0.6 °C between each other. Comparative uncertainty was measured by taping the tips of the three thermocouples together and submersing them in the water at varying temperatures: room-temperature, hot (above the highest temperature we measured in the experiment), and cold (below the minimum temperature). The maximum difference between measured outputs at any of these conditions was taken as the comparative uncertainty [24]. Outlet probes were inserted into the PVC tube through the epoxy to 3 cm away from the outlets before the epoxy hardened. Omega PX409 pressure transducers arranged at pipe cross-connections measured pressure at the inlet and outlets and have accuracies of ±0.08% BSL. Alicat MCR-500 flowmeters were utilized to record flowrates at the inlet and cold outlet at accuracies of ±(0.2%FS+0.8%Reading), with the full scale being 500 SLPM. Temperature and pressure data were collected using an NI cDAQ 9174 Chassis with NI 9212 mini-thermocouple reader and NI 9205 Voltage input reader for pressure. The cold flow fraction was controlled via backpressure by a globe valve on the hot end.

The miniature vortex tube was tested experimentally with room-temperature (18–24 °C, see Fig. 5) compressed air over a range of

Fig. 3 (*a*) Additively manufactured vortex tube compared to (*b*) USB memory stick

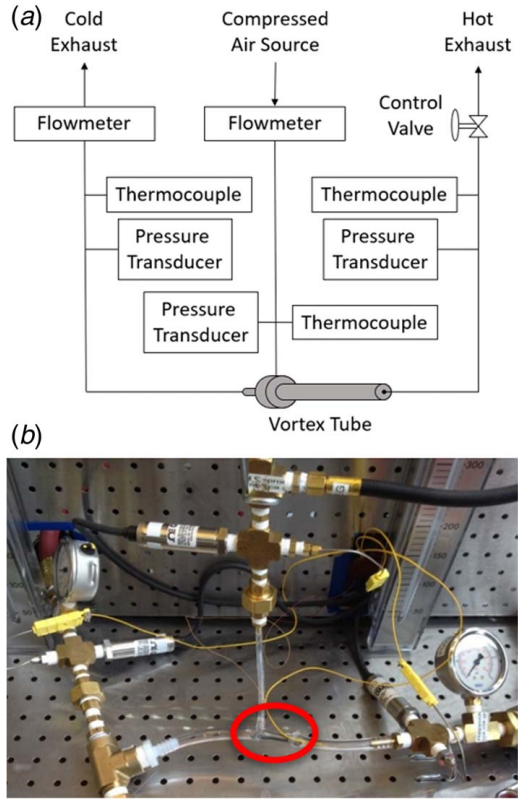

Fig. 4 (*a*) Diagram and (*b*) photograph of the testing setup with miniature vortex tube circled

cold fractions between 0 and 1 and at pressure ratios of 2, 3, and 4. The cold outlet was at the ambient pressure, approximately 93 kPa. Pressure ratios are specified using the cold outlet because the hot outlet is at somewhat elevated pressure.

The testing procedure was as follows. Compressed air regulated to the desired pressure was first applied to the inlet to begin testing, then the globe valve at the hot end was adjusted until a cold fraction of approximately 0.5 was obtained. Data points were taken first with decreasing cold fraction. Then, a second data point at a cold fraction near 0.5 was recorded before increasing cold fraction, and more data points were recorded. Alternatively, cold fraction could be increased first and decreased after. Finally, one more measurement was made at a cold fraction of 0.5. The three points at this cold fraction were compared with confirm similar performance from start to finish.

For each data point, time was allowed for the outlet temperatures to reach a steady-state. We define steady-state as the point where the

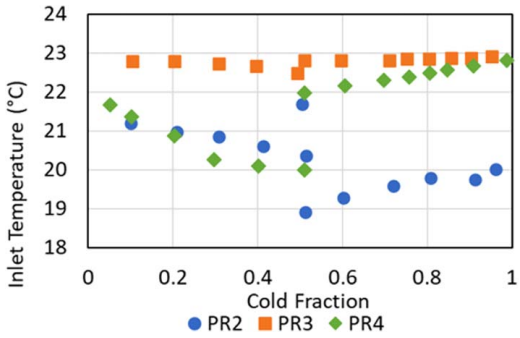

Fig. 5 Inlet temperature at pressure ratios of 2, 3, and 4 and cold fractions from 0 to 1. Temperatures tended to initially be low, but increase over time as the building's air compressor was used.

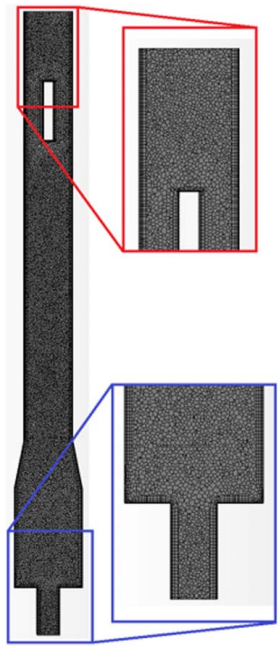

Fig. 6 Numerical mesh in the longitudinal cross sections of the whole tube (left), near the hot outlet (top right), and near the cold outlet (bottom right)

temperature does not change more than 0.1 °C in 2 min, usually taking 5–10 min per data point. Each data point consists of an average of about 15 individual readings in the steady-state regime.

In preliminary testing, it was noticed that adding insulation around the vortex tube increased the total temperature separation (T_{hot}–T_{cold}) by 18% at a cold fraction of 0.55. In subsequent tests, the vortex tube was wrapped in loose-knit cellulose fiber to act as insulation.

Computational Approach

The experimental results for the 3D-printed vortex tube were compared to those obtained via CFD simulations. Software STAR-CCM+ was used for CFD, employing Reynolds-averaged Navier–Stokes (RANS) approach and ideal air as a working fluid. The motivation for conducting computational studies is to determine whether CFD can be used for the confident design of vortex tubes.

The governing Reynolds-averaged equations include the mass, momentum, and energy equations:

$$\frac{\partial(\rho\bar{u}_j)}{\partial x_j} = 0 \tag{1}$$

$$\frac{\partial(\rho\bar{u}_i\bar{u}_j)}{\partial x_j} = -\frac{\partial p}{\partial x_i} + \frac{\partial}{\partial x_j}\left[\mu\left(\frac{\partial\bar{u}_i}{\partial x_j} + \frac{\partial\bar{u}_j}{\partial x_i} - \frac{2}{3}\delta_{ij}\frac{\partial\bar{u}_k}{\partial x_k}\right) - \rho\overline{u_j' u_j'}\right] \tag{2}$$

$$\frac{\partial(\rho E\bar{u}_j)}{\partial x_j} = \frac{\partial}{\partial x_j}\left[-p\bar{u}_i\delta_{ij} + u_i\left\{\mu\left(\frac{\partial\bar{u}_i}{\partial x_j} + \frac{\partial\bar{u}_j}{\partial x_i} - \frac{2}{3}\delta_{ij}\frac{\partial\bar{u}_k}{\partial x_k}\right) - \rho\overline{u_i' u_j'}\right\}\right] - \frac{\partial q_j}{\partial x_j} \tag{3}$$

where $\bar{u}_i$ are the time-averaged velocity components, p is the pressure, ρ is the fluid density, μ is the fluid viscosity, $-\rho\overline{u_i' u_j'}$ is the turbulent stress tensor, and q_j are the heat fluxes.

To model the turbulent stress, the elliptic-blending lag k–ε model [13] was applied as it demonstrated the best agreement with our test

data. Moreover, the two-layer, all Y+ variant of the turbulence model [25] was employed due to significant flow variability in the vortex tube. Other turbulence models were tried as well and their predictions are compared in the Results section. The specific implementation details of the numerical methods in the applied software can be found in Ref. [22].

The unstructured numerical grid was built inside the domain, as shown in Fig. 6, containing polyhedral cells that work well in situations with complex flows. Near the solid walls, five prismatic cell layers were constructed to cover the boundary layer. Because of high variations of the flow velocity inside vortex tubes and the associated difficulty of ensuring the same cell thickness in terms of Y+ values, the two-layer all-Y+ option was activated in all simulations. This approach allows resolving a viscous sub-layer when the cell thickness corresponds to Y+ below 5, while relying on wall functions for Y+ values above 30 and using a combined model for intermediate Y+ values. During simulations, maximum wall Y+ values remained less than 100 for all cells.

The grid independence study was carried out for conditions at a cold fraction of 0.5 with a pressure ratio of 3 and an inlet temperature of 23 °C. The total temperature difference between the hot and cold outlets and the temperature differences between the outlets and the inlet are shown in Fig. 7 as a function of the cell count in numerical simulations. Numerical results demonstrate convergence at sufficiently high mesh density with insignificant improvement between 505 K and 847 K cells. For subsequent simulations, grids with 505 K cell counts were employed.

Results

In the experimental parametric tests, the air flowrate increased with pressure ratio, with 14 SLPM (0.3 g/s) at a pressure ratio of 2, with 25 SLPM (0.5 g/s) at a pressure ratio of 3, and 35 SLPM (0.7 g/s) at a pressure ratio of 4. Experimental results for the outlet temperature variations as functions of cold fraction and pressure ratio are given in Fig. 8. The observed trends are typical for vortex tubes: the largest temperature drop at the cold outlet occurs at relatively low cold flow fraction when only the coldest fluid close to the tube centerline exits through this port, while the largest heating at the peripheral outlet happens at large cold fractions when only fluid closest to the tube wall leaves through that outlet. The magnitudes of temperature variations increase with pressure ratio due to higher flow velocities and thus larger shear work performed by the core flow on the outer flow inside the tube.

The most significant temperature separations were measured at a pressure ratio of 4 ± 0.1 with a cold drop of 13.3 ± 0.6 °C at a cold fraction of 0.20 ± 0.03 and a hot rise of 20.6 ± 0.6 °C at a cold fraction of 0.91 ± 0.05. Uncertainties take into account instrument error, DAQ uncertainty (if used), and random error, and thermocouple uncertainties are relative to each other. Isenthalpic expansion (throttling) could not have caused more than 1 °C of cooling in these conditions. The isentropic temperature efficiency, defined as a ratio of the measured temperature drop to that in the isentropic expansion process, is approximately equal to 14% at the coldest temperature condition.

Commercially available vortex tubes can achieve larger temperature separations than observed in this study; for example, a temperature drop at the cold outlet down to about 50 °C is possible at a pressure ratio of 4. However, commercial vortex tubes are several times larger in size and have been optimized, while the studied here tube is the first demonstrator of an additively manufactured vortex tube. A smaller tube size is also expected to degrade cooling performance, but the scale effect is not known.

One of the most important practical metrics of vortex tubes is the cooling power that can be approximated as follows:

$$\dot{Q} = \dot{m} c_p \Delta T \tag{4}$$

where $\dot{Q}$ is the cooling power produced, $\dot{m}$ is the mass flowrate through that outlet, c_p is the specific heat at constant pressure (taken to be 1.006 kJ/kg K), and ΔT is the temperature drop from the inlet to the cold outlet. As seen in Fig. 9, the cooling power peaks at larger cold fractions than for the maximum cooling temperature (Fig. 8), since cooling is proportional to both cold flow fraction and temperature separation. In the present setup, maximum cooling power was measured at a cold fraction of 0.6. At very low or very high cold fractions, the cooling power is minimal, since either the flow through the cold outlet decreases or the temperature drop becomes small.

An energy balance can be performed on the experimental system. It is assumed to be at steady-state with no work or heat transferring from/to the tube. Percent energy error can thus be calculated using the following equation with a positive value indicating energy has been lost from the system and a negative indicating energy was gained,

$$\%\dot{E}_{error} = \frac{\dot{m}_{in} h_{in} - \dot{m}_c h_c - \dot{m}_h h_h}{\dot{m}_{in} h_{in}} * 100\% \tag{5}$$

where $\%\dot{E}_{error}$ is the rate of energy error as a percentage of the inlet energy flow and h is the specific stagnation enthalpy at the system boundaries. Estimated with Eq. (5), the percent energy error was found to be less than 0.30% at all data points taken.

Computational simulations of this vortex tube were first run at the pressure ratio of 3, the cold fraction near 0.5, and the inlet temperature and pressure corresponding to the experimental conditions. An example of the numerically predicted total temperature field and the flow pattern in the longitudinal cross section of the vortex tube is illustrated in Fig. 10. (The images are shown in the vertical orientation only for compactness; gravity was not activated in CFD

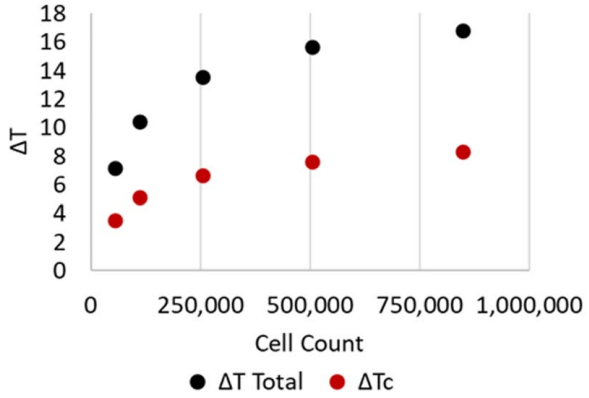

Fig. 7 Convergence of numerical results for magnitude of temperature separations with increasing number of cells. Cold fraction near 0.5 and pressure ratio of 3.

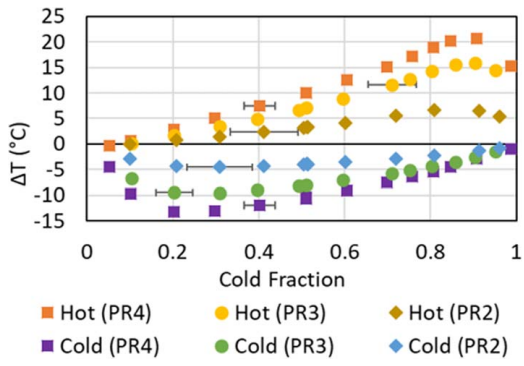

Fig. 8 Experimental results of total temperature changes (ΔT) from the inlet to the hot and cold outlets across cold fractions from 0 to 1 and pressure ratios (PR) of 2, 3, and 4. Uncertainties of temperature differences are 0.6 °C.

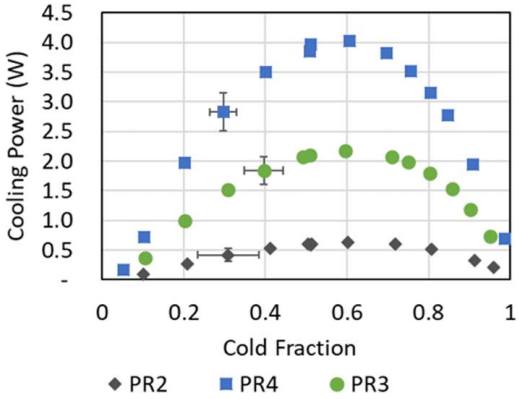

Fig. 9 Experimental cooling power across cold fractions from 0 to 1 and pressure ratios (PR) of 2, 3, and 4

simulations.) A slight asymmetry in the temperature profile can be seen, resulting from the asymmetry of the single inlet. Otherwise, the temperature increases toward the outer surface of the tube and toward the hot end (Fig. 10(*a*)). The coldest region is in the center of the vortex and close to the cold outlet (Fig. 10(*b*)). This region is effectively encapsulated by the wider-diameter section of the tube, where the vortex intensity is significantly higher, as also seen from the velocity field in Fig. 10. As the fluid moves to the tube section with narrower diameter, the velocity decreases, and temperature increases. The velocity shows considerable asymmetry for the same reason and is highest at the inlet (in the lower-left corner in Fig. 10) and decreases toward the center of the tube and toward the hot end (top). Maximum velocity in this cross section was 319 m/s, and the lowest total temperature was 11.2 °C. Percent errors in the energy balance of the computational models were found to be below 0.15% in all cases and below 0.025% in most cases.

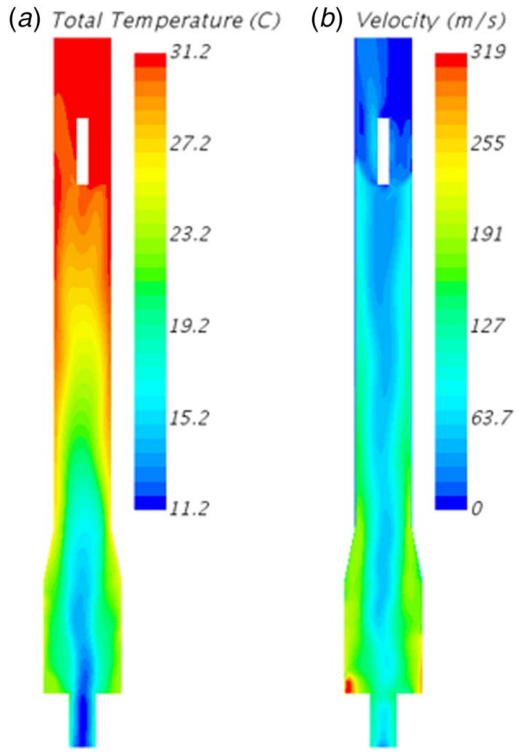

Fig. 10 (*a*) Total temperature distribution in °C and (*b*) velocity field in m/s inside the vortex tube simulated by CFD at a pressure ratio of 3 and cold fraction near 0.5

Table 1 Experimental (Exp) and numerical total temperatures at pressure ratio of 3 and cold fractions near 0.5. Numerical turbulence models include Elliptic-Blending Lag k–ϵ (EBL), Standard k–ϵ (Std), and k–ω Wilcox (k–ω)

	Exp	EBL	Std	k–ω
T_{in} (°C)	22.8	22.8	22.8	22.8
T_{cold} (°C)	14.8	15.2	9.3	10.5
T_{hot} (°C)	29.9	30.8	37.0	35.8
ΔT_{cold} (°C)	−8.0	−7.6	−13.5	−12.3
ΔT_{hot} (°C)	7.1	8.0	14.2	13.0

A reasonable agreement was obtained between numerical simulations using the elliptic-blending lag model and experimental observations at the selected setpoint with a cold fraction near 0.5 and a pressure ratio of 3. Differences between the simulation and experiment for the cold temperature drop and hot temperature rise were 5% and 13%, respectively (Table 1). Other turbulence models were also compared, such as standard k–ϵ and k–ω Wilcox models, producing much larger errors of 60–100%. This confirms the advantages of the elliptic-blending lag model for confined turbulent flows with high rotation and heat transport.

Further conditions were simulated computationally using the elliptic-blending lag k–ϵ model to obtain performance curves at pressure ratios of 3 and 4 and compared with experimental data (Figs. 11 and 12). At both pressure ratios and across the cold fractions, models agreed well to experiment except above cold fractions of 0.8, where CFD predicts a continuous rise in hot outlet temperature but experimental temperatures begin to drop and at cold fractions below 0.2, where numerical results do not show as significant of a drop-off in cooling at lower cold fractions. For example, at a pressure ratio of 3 and a cold fraction of 0.5, the cold outlet temperature drop was 8.0 °C in the experiment and 7.6 °C in the CFD, a difference of 5%. However, at a cold fraction of 0.1, they were 6.7 °C and 9.1 °C, respectively, a difference of 36%. Situations with extreme cold flow fractions may lead to the formation of pronounced secondary vortices, modeling of which may require finer mesh or more advanced approaches, such as the large-eddy simulation. Nevertheless, it can be concluded that the elliptic-blending lag k–ϵ model works reasonably well in a broad range of vortex-tube operational conditions.

Conclusion

A miniature, additively manufactured vortex tube with a cyclonic vortex chamber was fabricated and successfully demonstrated large temperature separations. With the pressure ratio of 4 and the flow-rate of 0.72 g/s, cooling by 13.3 °C was achieved at a cold fraction of 0.20 and heating by 20.6 °C was achieved at a cold fraction of 0.91. Additionally, CFD simulations using the elliptic-blending lag k–ϵ turbulence model were found to agree well to the

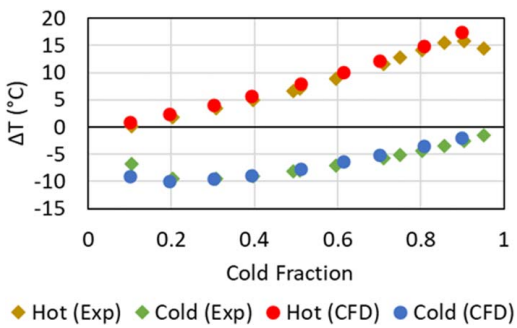

Fig. 11 Experimental (Exp) and computational (CFD) outlet temperatures at a pressure ratio of 3 over cold fractions of 0 to 1

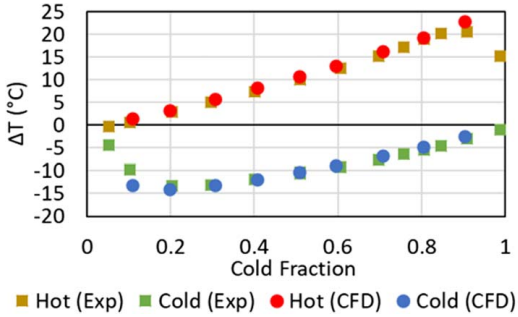

Fig. 12 Experimental (Exp) and computational (CFD) outlet temperatures at a pressure ratio of 4 over cold fractions of 0 to 1

experiment. Given the large temperature separations generated by the 3D-printed variable-diameter vortex tube, this type of vortex tube holds promise at room temperature. The intended next goal of this work will be to explore applications of additively manufactured vortex tubes in cryogenic hydrogen systems.

Acknowledgment

The authors thank Professor Amit Bandyopadhyay of Washington State University for allowing us to use his additive manufacturing facilities.

Funding Data

- This work was supported by the US Department of Energy under research contract No. DE-EE0008429.

Conflict of Interest

There are no conflicts of interest.

Data Availability Statement

The datasets generated and supporting the findings of this article are obtainable from the corresponding author upon reasonable request. The authors attest that all data for this study are included in the paper.

Nomenclature

h = specific stagnation enthalpy
p = pressure
q = heat flux
u = velocity
E = net energy
T = temperature
$\dot{m}$ = mass flow rate
$\dot{Q}$ = cooling power
c_p = specific heat at constant pressure
x_i = spatial coordinate
μ = viscosity
ρ = density

References

[1] Skye, H. M., Nellis, G. F., and Klein, S. A., 2006, "Comparison of CFD Analysis to Empirical Data in a Commercial Vortex Tube," Int. J. Refrig., **29**(1), pp. 71–80.
[2] Polihronov, J. G., and Straatman, A., 2012, "Thermodynamics of Angular Propulsion in Fluids," Phys. Rev. Lett., **109**(5), p. 054504.
[3] Merkulov, A. P., 1969, *The Vortex Effect and its Application in Technology*, Mashinostroenie, Moscow (in Russian). English translation: Merkulov, A.P., 1975, *The Vortex Effect and its Application in Technology*, U.S. Army Mobility Equipment R&D Center, Fort Belvoir, Virginia, T-1975-70.
[4] Kurosaka, M., 1982, "Acoustic Streaming in Swirling Flow and the Ranque-Hilsch (Vortex-Tube) Effect," J. Fluid Mech., **124**, pp. 139–172.
[5] Ranque, G. J., 1933, "Experiences sur la Detente Avec Production Simultanees D'un Echappement D'air Chaud et Echappement D'air Froid," J. Phys. Rad., **7**(4), pp. 112–115.
[6] Hilsch, R., 1947, "The Use of the Expansion of Gases in a Centrifugal Field as Cooling Process," Rev. Sci. Instrum., **18**(2), pp. 108–113.
[7] Saidi, M. H., and Valipour, M. S., 2003, "Experimental Modeling of Vortex Tube Refrigerator," Appl. Therm. Eng., **23**(15), pp. 1971–1980.
[8] Balmer, R. T., 1998, "Pressure-Driven Ranque-Hilsch Temperature Separation in Liquids," ASME J. Fluid Eng., **110**(2), pp. 161–164.
[9] Boswell, B., and Chandratilleke, T. T., 2009, "Sustainable Metal Cutting," Proceedings of the IEEE International Conference on Science and Technology for Humanity, Toronto, Canada.
[10] Yalcin, B., Ozgur, A. E., and Koru, M., 2009, "The Effects of Various Cooling Strategies on Surface Roughness and Tool Wear During Soft Materials Milling," Mater. Des., **30**(3), pp. 896–899.
[11] Rahman, S. M. H., and Saidur, R., 2016, "A Novel Atmospheric Freeze Dryer Using Simultaneous Application of Subzero and Hot Air Streams Using a Vortex Chiller," Drying Technol., **34**(12), pp. 1406–1413.
[12] Ahlborn, B. K., and Gordon, J. M., 2000, "The Vortex Tube as a Classic Thermodynamic Refrigeration Cycle," J. Appl. Phys., **88**(6), pp. 3645–3653.
[13] Bej, N., and Sinhamahapatra, K. P., 2014, "Numerical Analysis on the Heat and Work Transfer Due to Shear in a Hot Cascade Ranque-Hilsch Vortex Tube," Int. J. Refrig., **68**, pp. 161–176.
[14] Dincer, K., Baskaya, S., and Uysal, B. Z., 2008, "Experimental Investigation of the Effects of Length to Diameter Ratio and Nozzle Number on the Performance of Counter Flow Ranque-Hilsch Vortex Tubes," Heat Mass Transfer, **44**(3), pp. 367–373.
[15] Dyskin, L. M., 1989, "Characteristics of a Vortex Tube With Detwisting of Cold Flow," J. Eng. Phys. Thermophys., **57**(1), pp. 756–758.
[16] Takahama, H., and Yokosawa, H., 1981, "Energy Separation in Vortex Tubes With a Divergent Chamber," ASME J. Heat Transfer, **103**(2), pp. 196–203.
[17] Matveev, K. I., and Leachman, J. W., 2019, "Numerical Investigation of Vortex Tubes With Extended Vortex Chambers," Int. J. Refrig., **108**, pp. 145–153.
[18] Dutta, T., Sinhamahapatra, K. P., and Bandyopdhyay, S. S., 2010, "Comparison of Different Turbulence Models in Predicting the Temperature Separation in a Ranque–Hilsch Vortex Tube," Int. J. Refrig., **33**(4), pp. 783–792.
[19] Eiamsa-ard, S., and Promvonge, P., 2007, "Review of Ranque-Hilsch Effects in Vortex Tubes," Renewable Sustainable Energy Rev., **12**(7), pp. 1822–1842.
[20] Revell, A. J., Benhamadouche, S., Craft, T., and Laurence, D., 2006, "A Stress-Strain Lag Eddy Viscosity Model for Unsteady Mean Flow," Int. J. Heat Fluid Flow, **27**(5), pp. 821–830.
[21] Lardeau, S., and Billard, F., 2016, "Development of an Elliptic-Blending Lag Model for Industrial Applications," Proceedings of the 54th AIAA Aerospace Sciences Meeting, San Diego, CA, AIAA Paper 2016-1600.
[22] STAR-CCM+ Manual, 2020. https://mdx.plm.automation.siemens.com/star-ccm-plus
[23] Bunge, C. D., Shoemake, E. D., Matveev, K. I., and Leachman, J., 2019, "Experimental Performance of a Catalyzed Vortex Tube with Cryogenic Hydrogen," Proceedings of the 23rd Cryogenic Engineering Conference and International Cryogenic Materials Conference, Hartford, CT.
[24] Taylor, B. N., and Kuyatt, C. E., 1994, *Guidelines for Evaluating and Expressing the Uncertainty of NIST Measurement Results*, National Institute of Standards and Technology, Gaithersburg, MD, NIST Technical Note 1297.
[25] Rodi, W., 1991, "Experience with Two-Layer Models Combining the k-ε Model with a One-Equation Model Near the Wall," Proceedings of the 29th Aerospace Sciences Meeting, Reno, NV, AIAA paper 91-0216.